Electromagnetic counterparts to structured jets from gravitational wave detected mergers

Gavin P. Lamb[⋆] and Shiho Kobayashi

Astrophysics Research Institute, LJMU, IC2, Liverpool Science Park, 146 Brownlow Hill, Liverpool L3 5RF, UK

ABSTRACT

We show the peak magnitude for orphan afterglows from the jets of gravitational wave (GW) detected black hole/neutron star – neutron star (BH/NS–NS) mergers highly depend on the jet half-opening angle θ_j. Short γ-ray bursts (GRBs) with a homogeneous jet structure and $\theta_j > 10°$, the orphan afterglow viewed at the typical inclination for a GW detected event, $38°$, are brighter at optical frequencies than the comparable macronova emission. Structured jets, where the energetics and Lorentz factor Γ vary with angle from the central axis, may have low-Γ components where the prompt emission is suppressed; GW electromagnetic (EM) counterparts may reveal a population of failed-GRB orphan afterglows. Using a Monte Carlo method assuming an NS–NS detection limit we show the fraction of GW-EM counterparts from homogeneous, two-component, power-law structured and Gaussian jets where the variable structure models include a wide low energy and Γ component: for homogeneous jets, with a $\theta_j = 6°$ and typical short GRB parameters, we find r-band magnitude $m_r \leq 21$ counterparts for ~ 13.6 per cent of GW detected mergers; where jet structure extends to a half-opening angle of $25°$, two-component jets produce $m_r \leq 21$ counterparts in ~ 30 per cent of GW detected mergers, power-law structured-jets result in ~ 37 per cent and Gaussian jets with our parameters ~ 13 per cent. We show the features in the light curves from orphan afterglows can be used to indicate the presence of extended structure.

Key words: gravitational waves – gamma-ray burst: general.

1 INTRODUCTION

The merger of binary neutron star (NS) systems or black hole (BH) neutron star systems is thought to be the progenitors of short gamma-ray bursts (GRB) (Narayan, Paczynski & Piran 1992; Mochkovitch et al. 1993; Bogomazov, Lipunov & Tutukov 2007; Nakar 2007; Berger 2014). The rapid accretion of a merger debris disc on to a compact object can power relativistic bipolar jets. Jet energy is initially dissipated internally producing the prompt gamma-rays of a GRB. The jet interacts with the ambient medium at later times and develops an external shock which expands and produces a broad-band afterglow (e.g. Piran 2004; Zhang & Mészáros 2004).

The inspiral and merger of an NS–NS or BH–NS system are caused by the emission of gravitational waves (GW). Such GWs are a target for ground-based GW detectors such as advanced LIGO, Virgo and KAGRA (Aso et al. 2013; Abbott et al. 2016). The merger of binary BH systems produced the advanced LIGO detections GW150914, GW151226, GW170104 and the 87 per cent confidence LVT151012 (Abbott et al. 2016, 2017). BH–BH merg-

ers are not expected to produce an electromagnetic (EM) counterpart, however see Connaughton et al. (2016); Ackermann et al. (2016); Savchenko et al. (2016); Verrecchia et al. (2017); various scenarios have been suggested (e.g. Loeb 2016; Perna, Lazzati & Giacomazzo 2016; Yamazaki, Asano & Ohira 2016; Zhang 2016). To maximize the science returns from GW astronomy the detection of an EM counterpart is essential; GW from NS–NS and BH–NS mergers should be detected within the next few years. GW detections of BH/NS–NS mergers will trigger a broad-band search for EM counterparts. However, short GRBs rarely occur within the range of GW detectors, ~ 300 Mpc for face-on NS–NS mergers (Abadie et al. 2010); this is possibly due to the high collimation of the prompt γ-ray emission, where ~ 0.5 per cent of jets with a half-opening angle $\theta_j \sim 6°$ would be inclined towards an observer, or a mismatch between short GRB peak energies and the *Swift* detection band makes detection more difficult. However, the afterglows from the merger jets may be observable as 'off-axis' orphans. Alternatively, a large fraction of the jets from such mergers may have no bright prompt emission due to a low bulk Lorentz factor (Lamb & Kobayashi 2016). More isotropic EM counterparts are often discussed to localize a large sample of GW events (e.g. Nakar & Piran 2011; Metzger & Berger 2012; Gao et al. 2013;

Nissanke, Kasliwal & Georgieva 2013; Kisaka, Ioka & Takami 2015; Metzger et al. 2015; Hotokezaka et al. 2016).

Other than the bipolar jets, numerical simulations of NS–NS and BH–NS mergers show sub- and mildly relativistic ejecta (e.g. Rosswog et al. 2000; Ruffert & Janka 2001; Yamamoto, Shibata & Taniguchi 2008; Kiuchi et al. 2010; Foucart et al. 2012; Deaton et al. 2013; Hotokezaka et al. 2013; Dietrich et al. 2015; Kawaguchi et al. 2016; Dietrich & Ujevic 2017; Ciolfi et al. 2017). Such ejecta is more isotropic in the case of an NS–NS merger and highly anisotropic for BH–NS mergers (Kyutoku et al. 2015). This merger ejecta can produce macronovae (also called kilonovae) from the decay of r-process nucleosynthesis products (e.g. Li & Paczyński 1998; Berger, Fong & Chornock 2013; Tanvir et al. 2013). Macronovae typically peak at red wavelengths with $\gtrsim 22$ magnitude for a source at 200 Mpc (Tanaka 2016). Radio flares are expected at much later times: 1–4 yr and ~ 1 mJy (Nakar & Piran 2011; Hotokezaka et al. 2016). Additionally, the jet must propagate through the merger ejecta, forming a cocoon that can collimate the outflow (Bromberg et al. 2011; Nagakura et al. 2014). A resultant cocoon-ejecta shock may give rise to X-ray or UV/optical emission (Lazzati et al. 2017; Nakar & Piran 2017). The jet will break out of the merger ejecta and continue to propagate into the ambient medium where the collimating pressure from the cocoon is lost. This transition can result in the jet becoming structured, i.e. the energy ϵ and bulk Lorentz factor Γ vary across the jet cross-section (e.g. Lipunov, Postnov & Prokhorov 2001; Rossi, Lazzati & Rees 2002; Zhang & Mészáros 2002). Low-Γ components of a structured jet will give rise to EM counterparts to an NS–NS or BH–NS merger without the bright prompt γ-ray emission. Given a GW detection from an NS–NS or BH–NS merger, jet external shock EM counterparts will be able to reveal the jet structure.

In Section 2, we describe the jet structures considered in this paper; in Section 3, we give details of the model used to estimate the observable emission at any inclination and show the results of our Monte Carlo; in Section 4, we discuss the various afterglow peak flux and peak time distributions; and in Section 5, we give concluding remarks and comment on the results implications to EM counterpart searches for GW detected compact stellar mergers.

2 JET STRUCTURE

Jet structure refers to the opening angle and energy distribution within a relativistic jet; the jets in GRBs are usually assumed to have a simple 'top-hat' or homogeneous jet structure where the energy per unit solid angle ϵ and the bulk Lorentz factor Γ are uniform until a sharp edge at the jet opening angle. Structured jets, where the energy distribution varies with angle from the centre, have been discussed in relation to long GRBs. The structure is a result of the jet breaking out from the stellar envelope (e.g. Lyutikov & Blandford 2002; Levinson & Eichler 2003; Zhang, Woosley & MacFadyen 2003; Zhang, Woosley & Heger 2004; Lazzati & Begelman 2005; Morsony, Lazzati & Begelman 2010; Pescalli et al. 2015). Alternatively, the structure can be a result of the jet formation mechanism (e.g. van Putten & Levinson 2003; Vlahakis, Peng & Königl 2003), an accretion disc forms that can launch a relativistic jet, either by the Blandford-Znajek (BZ) mechanism (Blandford & Znajek 1977) or neutrino annihilation (e.g. Popham, Woosley & Fryer 1999). If the jet from an NS–NS or BH–NS merger propagates through an outflow at early times, then upon break-out some structure can be expected; similarly, if the jet is formed and accelerated by either BZ or neutrino annihilation, or a combination of both, then the structure can arise from the various components, i.e. spine and

sheath. Such jet structure could enhance the GW–GRB association probability (e.g. Jin et al. 2017; Kathirgamaraju, Barniol Duran & Giannios 2017).

Other than homogeneous jets, there are three alternative jet structures that are commonly discussed (e.g. Granot et al. 2002; Wei & Jin 2003; Panaitescu 2005):

(i) A two-component or spine and sheath jet: a fast, narrow core and slower, wider sheath (e.g. Vlahakis et al. 2003; Peng, Königl & Granot 2005; Jin et al. 2007). Also see Barkov & Pozanenko (2011), where the wide;r component is faster. Alternatively, baryon loading of the jet edges where a structured magnetic field prevents charged baryon drift into the jet core, will create a jet with uniform energy but a wider low-Γ component (Lei, Zhang & Liang 2013). The general two-component jet ϵ and Γ follow

$$\epsilon(\theta) = \begin{cases} \epsilon_c & \theta < \theta_c, \\ \epsilon_s & \theta > \theta_c, \end{cases} \qquad \Gamma(\theta) = \begin{cases} \Gamma_c & \theta < \theta_c, \\ \Gamma_s & \theta > \theta_c, \end{cases} \tag{1}$$

where the subscript c indicates the jet core parameter and the subscript s indicates the uniform sheath parameter.

(ii) A structured jet where the energy and Lorentz factor are a function of the jet angle outside a uniform core (e.g. Rossi et al. 2002, 2004; Zhang & Mészáros 2002; Kumar & Granot 2003). The jet ϵ and Γ follow

$$\epsilon(\theta) = \begin{cases} \epsilon_c & \theta < \theta_c, \\ \epsilon_c \left(\frac{\theta}{\theta_c}\right)^{-k_e} & \theta > \theta_c, \end{cases} \qquad \Gamma(\theta) = \begin{cases} \Gamma_c & \theta < \theta_c, \\ \Gamma_c \left(\frac{\theta}{\theta_c}\right)^{-k_\Gamma} & \theta > \theta_c, \end{cases} \tag{2}$$

where θ is the angle from the jet axis and we assume uniform baryon loading where $k_e = k_\Gamma = k \geq 0$.

(iii) A Gaussian jet (e.g. Kumar & Granot 2003; Rossi et al. 2004; Zhang & Mészáros 2004). The jet ϵ and Γ follow

$$\epsilon(\theta) = \epsilon_c e^{-\left(\theta^2/2\theta_c^2\right)}, \qquad \Gamma(\theta) = \Gamma_c e^{-\left(\theta^2/2\theta_c^2\right)}. \tag{3}$$

In all cases $\theta < \theta_j$, where θ_j is the maximum jet half-opening angle. The existence of a jet edge is motivated by numerical simulations of compact stellar mergers (e.g. Rezzolla et al. 2011), where resistive-magnetohydrodynamics simulations result in a jet-like magnetic structure with a half-opening angle of $\sim 25°$ (Dionysopoulou, Alic & Rezzolla 2015). The jets are assumed to be symmetric about the central axis. Observed emission from the various components of a jet depends on the viewing angle $\theta_{\rm obs}$, measured from the jet-axis.

3 METHOD AND RESULTS

The jet energy dissipated by internal processes (e.g. Rees & Meszaros 1994; Zhang & Yan 2011) is radiated as gamma-rays via the synchrotron process. The radius of this internal dissipation from the central engine can be estimated using the minimum variability of the prompt emission, typically $\delta t \sim 0.1$ s (Nakar & Piran 2002),

$$R_\gamma \simeq \Gamma^2 c\delta t \simeq 3 \times 10^{13} \delta t_{-1} \Gamma_2^2 \text{ cm}, \tag{4}$$

where c is the speed of light, $\delta t_{-1} = \delta t/0.1$ s and $\Gamma_2 = \Gamma/100$.

The optical depth τ of the relativistic jet plasma is less than unity at radii greater than the photospheric radius $R_{\rm p}$. A conservative estimate for the minimum photospheric radius can be made by considering the electrons that accompany baryons in the jet. By considering the scattering of photons by these electrons the optical depth can be estimated (e.g. Lithwick & Sari 2001). At a radius

R the optical depth would be $\tau = \sigma_{\text{T}} E / \left(4\pi R^2 m_{\text{p}} c^2 \Gamma\right)$, where σ_{T} is the Thomson cross-section, $E = 4\pi\epsilon$ is the isotropic equivalent blast energy and m_{p} is the mass of a proton. The radius where $\tau = 1$ is the photospheric radius

$$R_{\text{p}} \simeq 6 \times 10^{13} E_{52}^{1/2} \Gamma_2^{-1/2} \quad \text{cm}, \tag{5}$$

where $E_{52} = E/10^{52}$ erg.

For a jet element with low-Γ the initial dissipation happens well inside the photosphere; due to the relativistic beaming effect the dynamics and emission for the element can be evaluated in the spherical model with isotropic equivalent energy $4\pi\epsilon$ and Γ. The gamma-rays of the prompt emission are injected into an optically thick medium and the photons can remain trapped. The thermal energy of these trapped photons will be converted back to jet kinetic energy (Kobayashi & Sari 2001; Kobayashi, Ryde & Mac-Fadyen 2002) and the prompt gamma-rays from this jet region would be suppressed. For an observer looking 'on-axis' at such a region, all the prompt emission could be suppressed, resulting in a failed GRB (Rossi et al. 2002).

For gamma-rays injected below the photosphere, the energy density is adiabatically cooled until the photons decouple at the photospheric radius. The decoupling/emission time for these photons will be delayed from the dissipation or energy injection time t_0. Dissipation occurs during the coasting phase of the jet where Γ is constant and temperatures are sub-relativistic (Piran, Shemi & Narayan 1993). As the energy density e evolves as $e \propto R^{-8/3}$, and the injected luminosity evolves as $L_\gamma \Delta/c \propto eR^2\Delta\Gamma^2$, where L_γ is the injected γ-ray luminosity and Δ is the shell width, the emitted gamma-ray luminosity at the photosphere $L_{\gamma,\text{p}}$ will be

$$L_{\gamma,\text{p}} \simeq L_\gamma (R_p/R_\gamma)^{-2/3} \quad \text{erg s}^{-1}. \tag{6}$$

Additional to the adiabatic cooling, the prompt photons will be Compton downscattered and thermalized; the efficiency of the thermalization depends on the depth below the photosphere and therefore the optical depth (Pe'er, Mészáros & Rees 2005; Thompson, Mészáros & Rees 2007). The high-energy spectrum will steepen and pair-production will determine a maximum spectral energy. The low-energy spectral slope will steepen due to Compton scatterings as the thermalization becomes more efficient.

A relativistic jet propagating into an ambient medium will decelerate when the swept-up mass is equivalent to M_0/Γ, where $M_0 = 4\pi\epsilon/\Gamma$ is the explosion rest mass. A forward and reverse shock form and synchrotron radiation produces the observed afterglow of GRBs (e.g. Rees & Meszaros 1992; Mészáros & Rees 1997; Kobayashi, Piran & Sari 1999; Sari & Piran 1999). The deceleration radius is $R_{\text{d}} \propto l/\Gamma^{2/3}$, where l is the Sedov length $l = \left(3E/4\pi m_{\text{p}} c^2 n\right)^{1/3}$. The observed deceleration time is then $t_{\text{d}} \propto E^{1/3} n^{-1/3} \Gamma^{-8/3}$.

A reverse shock will propagate through the ejecta from the central engine at the beginning of the decelerating blastwave phase. The reverse shock contains energy comparable to the forward shock but due to a higher mass, the peak frequency is lower by a factor $\sim\Gamma^2$ (Kobayashi & Zhang 2003). High polarization measurements in the afterglow of long GRBs suggest magnetized jets (Steele et al. 2009; Mundell et al. 2013), these observations still support a baryonic jet rather than a Poynting flux dominated jet, although a strong magnetic field can suppress the reverse shock. The reverse shock emission associated with short GRBs is rarely observed, either due to the early time of the peak, the typical frequency well below optical, or due to magnetic suppression. We consider only the forward shock emission in this paper.

3.1 Numerical model

Jet parameters used throughout this paper are bulk Lorentz factor $\Gamma = 100$, ambient number density $n = 0.1 \text{ cm}^{-3}$, microphysical parameters $\varepsilon_{\text{B}} = 0.01$, $\varepsilon_{\text{e}} = 0.1$, γ-ray efficiency $\eta = 0.1$ and minimum variability time-scale $\delta t = 0.1$ s; the isotropic equivalent jet kinetic energy is $E_{\text{k}} = E_{\text{iso}}(1 - \eta)$. We have used an isotropic equivalent blast energy of $E_{\text{iso}} = 4\pi\epsilon_{\text{c}} = 2 \times 10^{52} \text{ erg s}^{-1}$; this value is taken from the peak of the $E_{\gamma,\text{iso}}$ distribution in Fong et al. (2015), and assuming our γ-ray efficiency. The blast energy value is consistent with that found for jets from mergers by Shapiro (2017) and for the break-point in the luminosity function for short GRBs found by Wanderman & Piran (2015).

To estimate the observed intensity of the emission from a relativistic source at a generic viewing angle, we consider the Lorentz invariant quantity I_ν/ν^3, where I_ν is the specific intensity and ν the frequency (Rybicki & Lightman 1979). As $\nu = \delta\nu'$, where $\delta = [\Gamma(1 - \beta\cos\alpha)]^{-1}$ is the relativistic Doppler factor, $\Gamma = (1 - \beta^2)^{-1/2}$ the bulk Lorentz factor and β the velocity as a fraction of the speed of light, α the inclination to the line of sight of the bulk motion, then $I_\nu = I'_{\nu'}\delta^3$, where primed quantities are in the comoving frame. By considering the observed on-axis emission, the specific flux to an off-axis observer will be a factor a^3 times the on-axis value, where $a = \delta(\alpha)/\delta(\alpha = 0) < 1$, i.e. $F_\nu(t, \alpha) = a^3 F_{\nu/a}(at, \alpha = 0)$ for a point source (Granot et al. 2002).

We model the prompt and afterglow emission from compact stellar merger jets by dividing the jet structure into $N \times M$ segments defined using spherical co-ordinates; the angle from the jet central axis is defined as $0 < \theta_i < \theta_j$ and the rotation around the jet central axis as $0 < \phi_k < 2\pi$. A segment has an opening angle of $\Delta\theta = \theta_j/N$ and an angular width $\Delta\phi = 2\pi/M$. The normal of each segment surface is θ_i from the central axis, where $\theta_i = (i - 1/2)\Delta\theta$, i is an integer in the range $1 \leq i \leq N$. Similarly, the rotation position is $\phi_k = (k - 1/2)\Delta\phi$, k is an integer in the range $1 \leq k \leq M$.

A segment has a bulk Lorentz factor and energy consistent with the jet structure model used; where for the jet structure models considered here, $\theta \ll \theta_{\text{c}}$ (i.e. the segment next to the jet axis) is used to normalize the energy distribution. Each segment has an energy per unit solid angle $\epsilon_{i,k}$ and a bulk Lorentz factor $\Gamma_{i,k}$. The energy dissipated as gamma-rays at the radius $R_\gamma \propto \Gamma_{i,k}^2$ is $L_{\gamma,i,k} \sim 4\pi\eta\,\epsilon_{i,k}/t_{\text{in}}$, where t_{in} is the energy injection time-scale i.e. the pulse duration of γ-ray emission from a segment. We assume that $t_{\text{in}} \equiv \delta t$; short GRBs often have multiple pulses, in such a case the duration of the prompt emission is longer than the variability time-scale $t_{\text{in}} > \delta t$, the choice of $t_{\text{in}} = \delta t$ results in bright GRBs and it gives conservative estimates for the orphan afterglow rates. The energy dissipated by each segment is then $t_{\text{in}} L_{\gamma,i,k} \Omega_{i,k}/4\pi$.

Prompt emission: The $EF_E \equiv \nu F_\nu$ spectrum for the injected photons is assumed to be a broken power law that peaks at E_{p} with a spectral index of 1.5 below the peak and -0.25 above the peak. The spectral peak follows the $L_\gamma - E_p$ relation $E_{p,i,k} \sim 300(L_{\gamma,i,k}/10^{52} \text{ erg})^{2/5}$ keV (Yonetoku et al. 2004; Ghirlanda et al. 2009; Zhang & Li 2012), where $L_{\gamma,i,k}$ is the isotropic equivalent γ-ray energy in the segment. For each segment the optical depth at R_γ is $\tau_{i,k} = (R_{\text{p}}/R_\gamma)^2$; if $\tau_{i,k} > 1$ then the photons will be coupled to the jet plasma until a radius R_{p} when $\tau_{i,k} = 1$ (Beloborodov 2011; Hascoët et al. 2014; Lamb & Kobayashi 2016). For cases where $\tau_{i,k} > 1$ at R_γ, the photon energy will be adiabatically cooled as $L_{\gamma,i,k}\tau_{i,k}^{-1/3}$; and the spectral peak energy will similarly reduce by a factor $\tau_{i,k}^{-1/3}$. The condition for efficient thermalization is, $\tau_{i,k} \geq m_{\text{e}}c^2/k_{\text{B}}T_{\text{BB}}$ (Pe'er et al. 2005; Thompson et al. 2007), where m_{e} is the mass of an electron, k_{B} is the

Boltzmann constant and T_{BB} is the electron blackbody temperature $T_{BB} = (L_{\gamma,i,k}/4\pi R_\gamma^2 \Gamma_{i,k}^2 c \, a_c)^{1/4}$, here a_c is the radiation constant. If this condition is met then the spectral peak energy is given by $\sim 3k_B T_{BB}$ and the spectrum is exponentially suppressed above this energy. If thermalization is not efficient, then the maximum spectral energy is limited by pair production; a cut-off in spectral energy occurs at $511(\Gamma_{i,k}/\tau_{i,k})$ keV.

For each segment, the luminosity and time-scales for an on-axis observer are determined using the fireball model. The on-axis luminosity and time are corrected for the angle from the segment to the observers line of sight. The emission time t_e for each segment depends on the point at which the photons decouple from the plasma. For segments where $\tau_{i,k} \leq 1$ this occurs at t_0; for segments where $\tau_{i,k} > 1$ then the emission is delayed so $t_e(\alpha = 0) = t_0 + (R_p - R_\gamma)/2\Gamma_{i,k}^2 c$. For an observer at θ_{obs} and ϕ_{obs}, the angle is $\alpha_{i,k}$. The emission time for segments at an angle $\alpha_{i,k}$ is delayed, so $t_e(\alpha) = a^{-1} t_e(\alpha = 0)$. Since the dissipated energy is radiated over an area $D_L^2 \Omega_{e,i,k}$, the on-axis flux is given by,

$$F_{\nu,i,k}(t, \alpha = 0) = \frac{L_{\nu,i,k}}{4\pi D^2} \frac{\Omega_{i,k}}{\Omega_{e,i,k}}, \qquad (7)$$

where $\Omega_{e,i,k} = \max[\Omega_{i,k}, \Omega_{\Gamma,i,k}]$ and $\Omega_{\Gamma,i,k}(t_{i,k}) = 2\pi(1 - \cos 1/\Gamma_{i,k})$ the beaming solid angle defined by the instantaneous segment bulk Lorentz factor. Similarly, the frequency of the emission is lowered, and the duration will be longer, by the factor a. The flux from each segment for an off-axis observer is given by,

$$F_{\nu,i,k}(t, \alpha_{i,k}) = a^3 \, F_{\nu/a,i,k}(at, \alpha = 0) \, \cos \alpha_{i,k}, \qquad (8)$$

where $\cos \alpha_{i,k}$ is the correction for the emission area projection (Salmonson 2003). The spectral peak is normalized as the value integrated between 1 keV and 10 MeV giving $L_{\gamma,i,k}$. The prompt emission is then the sum of each segments emission in a time bin between t_0 and the maximum emission time $a^{-1}(t_e + t_{in})$. The burst is detected if the number of photons at the detector is >0.2 ph s^{-1} cm^{-2} in the *Swift* band, 15–150 keV (Band 2006).

Afterglow emission: Jet energy that is not radiated away by the prompt emission drives a relativistic outflow into the interstellar medium. The kinetic energy per unit solid angle of a jet segment is $\epsilon_{k,i,k} = \epsilon_{i,k} - t_{in} L_{\gamma,i,k}/4\pi$. We assume no sideways expansion so each jet segment evolves independently (van Eerten & MacFadyen 2012); the lateral expansion of homogeneous and structured jets is discussed by Salmonson (2003). The value of $\Gamma_{i,k}$ is considered constant, $\Gamma_{0,i,k}$, before the deceleration radius R_d and will evolve as $\Gamma_{0,i,k}(R_{i,k}/R_d)^{-3/2}$ with distance $R_{i,k}$ when $R_{i,k} > R_d$. The on-axis flux from each segment at a given observer time t can be evaluated by using the standard synchrotron shock model. The on-axis characteristic frequency ν_m and cooling frequency ν_c are calculated in the same way as discussed in Sari, Piran & Narayan (1998). The peak flux of the afterglow is obtained by considering the total number of electrons in the segment $N_e = nR^3\Omega_{i,k}/3$. The total energy per unit time per unit frequency emitted by these electrons is proportional to $N_e \propto \Omega_{i,k}$ and is distributed over an area $D_L^2 \Omega_{e,i,k}$ at a distance D_L from the source. Since the on-axis peak flux density $F_{\nu,max}$ is proportional to $\Omega_{i,k}/\Omega_{e,i,k}$, we obtain the on-axis flux from a segment $F_{\nu,i,k}(t, \alpha = 0) = F_\nu(t) \Omega_{i,k}/\Omega_{e,i,k}$ where $F_\nu(t)$ indicates the flux from a blast wave with the isotropic energy $4\pi\epsilon_{k,i,k}$ (Sari, Piran & Narayan 1998; Sari, Piran & Halpern 1999). For an off-axis observer the flux from a segment is given by equation (8); the sum of flux from each segment at time t gives a total afterglow light curve. Using this model the emission from a decelerating jet can be estimated at various observation angles.

3.2 Homogeneous jets: approximations

Here, we give an approximation for the peak flux and peak time of an orphan afterglow from a homogeneous jet; the estimates will be compared with the numerical results. The afterglow emission from a decelerating relativistic collimated blastwave is beamed within the angle $\theta_j + 1/\Gamma$. For observers outside this angle, the emission becomes much fainter as the inclination of the system increases. Assuming slow cooling with $\nu_m < \nu < \nu_c$, and the Doppler correction for an off-axis observer, the observed peak flux is approximately,

$$F_p = C(p) \, f(\theta_{obs}, \theta_j) \, [\theta_{obs} - \theta_j]^{2(1-p)} \, \nu^{(1-p)/2}$$
$$\times E_k \, n^{(1+p)/4} \, \varepsilon_B^{(1+p)/4} \, \varepsilon_e^{p-1} \, D^{-2} \quad \text{erg s}^{-1} \text{ cm}^{-2} \text{ Hz}^{-1}, \qquad (9)$$

where $C(p)$ is a constant that depends on the particle index p and all the relevant physical parameters,[1] $f(\theta_{obs}, \theta_j)$ accounts for the jet opening angle θ_j, viewing angle θ_{obs} and the relativistic beaming, and ν is the observed frequency. The factor $f(\theta_{obs}, \theta_j)$ is,

$$f(\theta_{obs}, \theta_j) = \cos(\theta_{obs} - \theta_j)$$
$$\times \left[\frac{1 - \cos\theta_j}{1 - \cos\left([(7-p)/(2p-2)]^{1/2}\theta_{obs}\right)} \right], \qquad (10)$$

where $\cos(\theta_{obs} - \theta_j)$ corrects for the surface area projection and the second term accounts for the emission solid-angle.

For $p = 2.5$, the peak flux is,

$$F_p \sim 2 \times 10^{-3} \, f(\theta_{obs}, \theta_j) \, [\theta_{obs} - \theta_j]^{-3} \, \nu_{14}^{-3/4}$$
$$\times E_{52} \, n_{-1}^{7/8} \, \varepsilon_{B,-2}^{7/8} \, \varepsilon_{e,-1}^{3/2} \, D_{200Mpc}^{-2} \quad \text{mJy}, \qquad (11)$$

where we use the convention $N_x = N/10^x$. Angles are in radians, frequency is in Hz, E is the isotropic jet kinetic energy E_k in erg, ambient number density n in cm^{-3} and the distance is normalized to 200 Mpc.

The peak flux occurs at a time given by,

$$t_p \sim 195 \left[\frac{(5+p)(7-p)^{1/3}}{(p-1)^{4/3}} \right] [\theta_{obs} - \theta_j]^{8/3} \, n_{-1}^{-1/3} \, E_{52}^{1/3} \quad \text{days}. \qquad (12)$$

The expressions in equations (11) and (12) give an approximation for the peak flux and time from an off-axis orphan afterglow to a relativistic jet with homogeneous structure in a uniform density ambient medium.

3.3 Monte Carlo results

Given a GW detection from an NS–NS or BH–NS merger, the fraction of events that have detectable EM counterparts from the relativistic jet depends on the jet structure and opening angle. Using a Monte Carlo method we estimate the fraction of merger jets, with a given jet structure, that result in EM counterparts brighter than r-band magnitude $m_r \leq 21$. A population of 10^5 mergers within the face-on detection limit for an NS–NS merger by advanced LIGO ~ 300 Mpc is generated. The luminosity distance D_L to a merger is randomly determined using the redshift distribution for non-collapsar short GRBs found by Wanderman & Piran (2015). The inclination i follows a random isotropic distribution.

---

[1] $C(p) = (32\pi)^{(1+p)/4} \quad (12\pi)^{-1} \quad (2\pi)^{(1-p)/2} \quad m_p^{(5p-7)/4} \quad m_e^{(5-3p)/2}$ $q_e^{(p-3)/2} \quad c \quad \sigma_T \quad [(2p-4)/(7-p)]^{p-1} \quad [(7-p)/(5+p)]^{(5+p)/2}$, where m_e is the electron mass, c the speed of light, σ_T the Thomson cross-section, q_e an electron charge and m_p the proton mass.
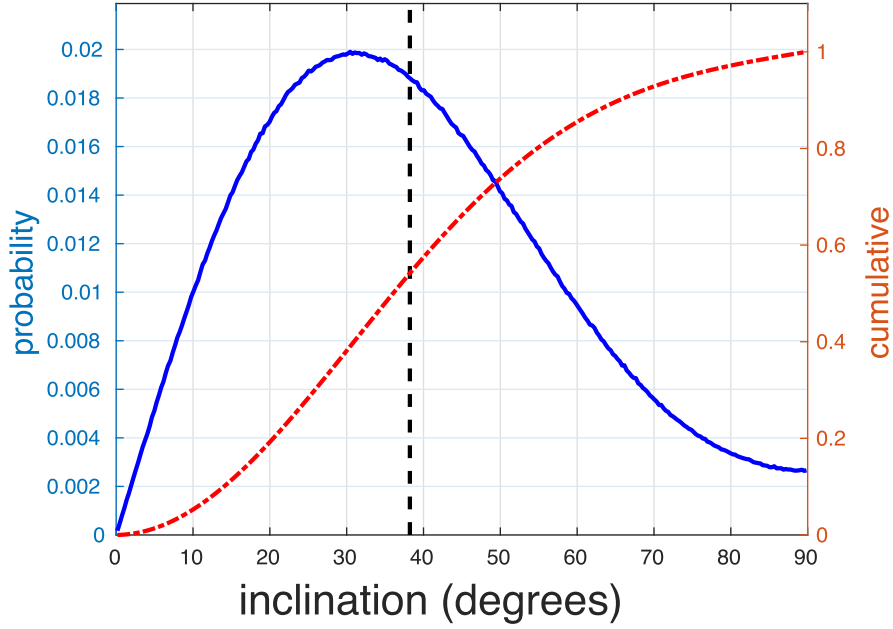
Figure 1. By considering the GW strain from a merger as a function of inclination, the distribution of system inclinations can be determined. For all GW detected mergers at a fraction of the maximum detectable luminosity distance, the probability of a system being inclined at given angle is shown with the blue solid line. The mean system inclination for this distribution is the dashed black line. The red dashed–dotted line is the cumulative distribution.

By considering that GW signals are stronger along the system rotation axis for binary mergers with a random orientation, the average inclination for a distribution of GW detected mergers can be determined. Mergers with a GW strain $h \propto (h_+^2 + h_\times^2)^{1/2}/D_L$, where $h_+ \propto 1 + \cos^2 i$ and $h_\times \propto 2\cos i$, are GW detected if $h > h_c$ the limiting detectable strain (e.g. Kochanek & Piran 1993; Lamb & Kobayashi 2016); for a more detailed investigation of the detectable gravitational waves from compact binary mergers (see Kobayashi & Mészáros 2003; Nissanke et al. 2010; Schutz 2011). The distribution of merger inclinations is shown in Fig. 1; the peak of the probability distribution is $i \sim 31°$ and the mean $\langle i \rangle \sim 38°$. The blue solid line is the probability of a merger with a given inclination; the red dash–dotted line is the probability that a merger will have an inclination equal or less than a given value.

The peak magnitude for an observer at the mean GW detection inclination angle of $\sim 38°$ from a homogeneous jet depends on the half-opening angle of the jet. By considering a homogeneous jet with a constant isotropic equivalent blast energy, or a constant geometrically corrected jet energy, the peak magnitude of the orphan afterglow for an observer at 200 Mpc and 38° can be estimated. Using the isotropic equivalent energy $E_{\rm iso} = 2 \times 10^{52}$ erg, or the geometrically corrected energy $E = E_{\rm iso}\Omega/2\pi = 3 \times 10^{50}$ erg, giving $E_{\rm iso}$ for a $\theta_j = 10°$, the peak magnitude for jet half-opening angles $2° \leq \theta_j \leq 30°$ are shown in Fig. 2. The thick red line is for constant $E_{\rm iso}$, and the thick blue dotted line for constant geometrically corrected jet energy. Three optical bands are shown, g, r and i band and the equivalent peak macronova flux, black dashed line, for an NS–NS merger (Tanaka et al. 2014). BH–NS mergers would result in brighter macronova, ~ 23.8, 23.2 and 22.8, respectively, although the ejecta in these cases is not isotropic. The macronova estimates should be considered as upper limits, for the adopted model, as the peak flux depends on the inclination where the brightest emission coincides with the polar axis (the jet axis) (Tanaka 2016; Wollaeger et al. 2017); however, macronova may be brighter than the adopted

model, i.e. Jin et al. (2016). The frequency dependence for the afterglow flux is shallower than that of a macronova which peaks sharply in the red to radio with a thermal spectrum and exponential decay at higher frequencies. The non-thermal spectrum of a GRB afterglow, where the higher frequency is typically $F_\nu \propto \nu^{-(p-1)/2}$ or $F_\nu \propto \nu^{-p/2}$, where $p \sim 2.5$, ensures that for an off-axis observer the afterglow is at a similar amplitude in a range of detection bands.

In Fig. 2, we see that the peak flux for an orphan afterglow viewed at 38° is brighter for homogeneous jets with wider jet half-opening angles. The point at which the peak flux for constant isotropic equivalent blast energy and constant geometrically corrected jet energy are equal indicates the normalization angle. For jets normalized to this value with narrower half-opening angles, the peak afterglows are brighter than the equivalent constant isotropic blast energy case; this is due to the jet having a higher energy density in these cases, for jets wider than this normalization, a reduction in jet energy density is apparent. The shape of the curve is dominated by the effective angle to the jet for wide θ_j i.e. $(\theta_{\rm obs} - \theta_j)^{-3}$ equation (11); and for narrower θ_j, by the fill factor, i.e. the second part of the expression in equation (10). For a jet with a given opening angle, inclination, distance and observation frequency the peak orphan afterglow flux is $F_p \propto E_k n^{7/8} \varepsilon_B^{7/8} \varepsilon_e^{3/2}$; the degeneracy in ε_B and n can make determination of these parameters difficult; the change in peak flux for a one order of magnitude change in any of these parameters is indicated by the length of the error bars in the third panel. Short GRBs often occur in low-density environments, a reduction in n by an order of magnitude would result in a peak that is $\Delta m_{\rm AB} \sim 2.2$ dimmer.

Within Fig. 2 the peak flux for the orphan afterglow of a two-component jet is shown as a thin red and a thin blue dotted line. In each case, the wider jet structure extends to 30° (equivalent to θ_j in equation 1) with energy and Lorentz factor at 5 per cent the value for the core region, defined by the *x*-axis in the figure. For the thin red line, the jet has an isotropic equivalent blast energy for
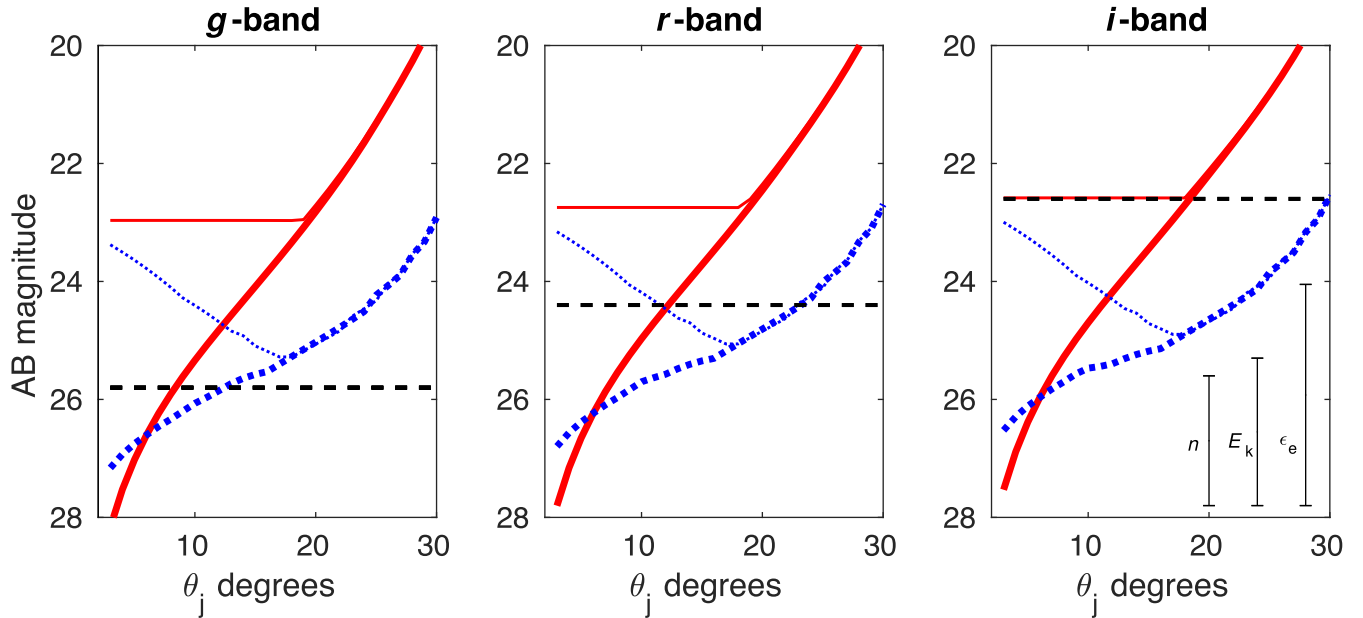
Figure 2. The peak magnitude for the off-axis afterglow at $38°$ from a homogeneous merger jet with opening angle θ_j at 200 Mpc. Red thick line indicates a jet with constant isotropic equivalent energy, $E_{iso} = 2 \times 10^{52}$ erg, and the blue thick dashed line indicates a jet with constant geometrically corrected jet energy (normalized to a $\theta_j = 6°$ jet with $E_{iso} = 2 \times 10^{52}$ erg). The thin lines indicate a two component jet, where θ_j defines the core angle (θ_c in equation 1) and the wider component extends to $30°$ (equivalent to θ_j in equation 1). The energy and Lorentz factor of the wide component are fixed at 5 per cent the core values. All jets have a core Lorentz factor of $\Gamma = 100$ and are in an ambient medium with a particle density of $0.1\,\mathrm{cm}^{-3}$. The full size of the error bars in the right-hand panel indicate the magnitude of change in peak flux for a one order of magnitude change in the respective parameter (note that n is degenerate with ε_B). The black dashed horizontal lines indicate the peak macronova emission for an NS–NS merger, assuming isotropic emission from a soft equation-of-state model, e.g. Tanaka et al. (2014) at 200 Mpc.

an on-axis observer $\theta_{obs} < \theta_c$ of 2×10^{52} erg; the thin dotted blue line has a constant geometrically corrected jet energy normalized to a homogeneous jet with an opening angle of $6°$. As the two-component jet always has a wide sheath that extends to $30°$, beyond the core angle defined by θ_j on the plot x-axis, the peak flux for jets with a core narrower than $\sim 20°$ is constant and approaches the homogeneous jet case for half-opening angles wider than this. By considering equation (11) for two homogeneous jets, one with fixed energy and undefined θ_j and the second with $\theta_j = 30°$ and 5 per cent the energy of the first, the θ_j for the more energetic jet that results in the same peak orphan afterglow for an observer at θ_{obs} is $\theta_j \sim \theta_{obs} - 20^{1/3}(\theta_{obs} - 30)$ deg. The wide sheath with 5 per cent the core energy and Lorentz factor is the dominant contributor to the off-axis emission for jets with a core $\lesssim 20°$. Where the jet energy is fixed at the geometrically corrected value for a $6°$ homogeneous jet, the reduction in the energy content of the wider component as the core width is increased leads to a dimmer afterglow. When the off-axis emission from the jet core becomes brighter than the off-axis emission from the sheath, the peak off-axis flux follows the homogeneous jet. Two-component jets are described in Section 2 and their afterglows discussed below.

The Monte Carlo distribution of mergers for each structure model have identical values of the core opening angle $\theta_c = 6°$. Hydrodynamic simulations indicate a range of jet core half-opening angles that are dependent on the initial conditions, $3° \lesssim \theta_c \lesssim 13°$ (Nagakura et al. 2014). The core value is significantly wider than the core values used in other structured jet models (e.g. Rossi et al. 2002; Salmonson 2003). The two-component jet has ϵ_s and Γ_s at 5 per cent the core values, while the power-law jet has an index $k = 2$ for

$\theta > \theta_c$. The effect of jet structure on the observed jet-break is discussed below. For the extended structure the minimum Γ is 2, and the maximum half-opening angle is $25°$, and all other parameters are as previously used.

Examples of the afterglow light curves for each model from a jet at 200 Mpc and viewed at inclinations from $0°$ to $40°$, in $5°$ intervals, are shown in Fig. 3; each jet structure has 120×120 segments. The light curve produced using $N = M = 120$ in the model is identical for values of $N, M > 120$; where $N, M < 120$ the peak flux and time for afterglows are consistently reproduced although the shape of the early afterglow before the peak is inaccurate. Off-axis light curve shape is generally unaffected by the reasonable choice of segment number. The blue lines indicate the afterglow for a *Swift* detectable GRB, $\theta_{obs} \leq 10°$; the red dashed lines indicate the afterglow for a jet viewed within the half-opening angle but without a *Swift* detectable GRB, a failed-GRB, $\theta_{obs} \leq \theta_j$; the black dash–dotted lines indicate an off-axis orphan afterglow, $\theta_{obs} > \theta_j$. For the homogeneous jet, the analytic peak magnitude and time from equations (11) and (12) are shown as blue crosses; the analytic expressions overestimate the peak flux and underestimate the peak time, when $\theta_{obs} \lesssim 3\theta_j$. Additional light curves are shown in the top-left panel for an observer at $0°$ and $10°$, blue dashed and black dotted lines, respectively. Here, the ambient number density is lower by a factor 10; for an on-axis observed afterglow, this parameter change results in a peak flux that is ~ 1.2 magnitudes fainter and for off-axis observed afterglow the peak flux is ~ 2.2 magnitudes fainter. A similar change in magnitude, $1.2 \lesssim \Delta m_r \lesssim 2.2$, is observed for all light curves where the ambient density is lower by a factor 10.
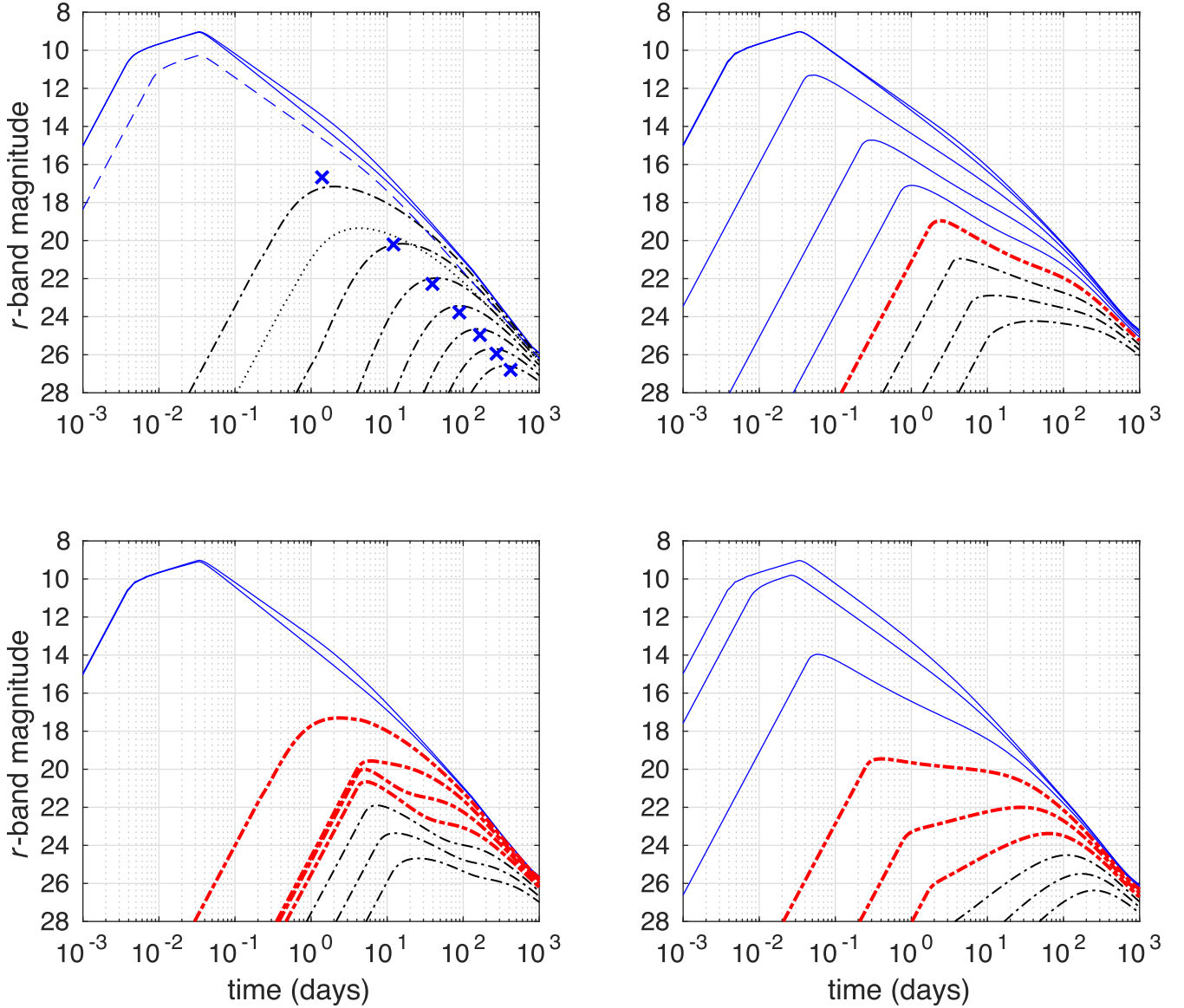
Figure 3. Afterlow *r*-band light curves for jets at 200 Mpc. Light curves are plotted for an observer at 5° increments in the range $0° \leq \theta_{obs} \leq 40°$. The model values used in each case are: (top left) $\theta_c = \theta_j = 6°$ for the homogeneous jet; (bottom left) $\theta_c = 6°$ for the two-component jet where the second component extends to $\theta_j = 25°$ with 5 per cent of the core energy and Lorentz factor; (top right) $\theta_c = 6°$ for the power-law jet with an index $k = 2$ for $\theta_c < \theta \leq 25°$; and (bottom right) $\theta_c = 6°$ for the Gaussian jet with a maximum $\theta_j = 25°$. Jets have an isotropic equivalent blast energy of 2×10^{52} erg, a bulk Lorentz factor $\Gamma = 100$ and an ambient medium density of $n = 0.1$. Blue lines indicate the afterglow of a GRB; red dashed lines indicate an on-axis orphan afterglow, i.e. within the wider jet opening angle but with suppressed prompt emission; black dashed–dotted lines indicate an off-axis orphan afterglow. The blue dashed and black dotted lines in the top-left panel indicate the afterglow for an observer at 0° and 10°, respectively, where the ambient medium has a particle density $n = 0.01$ cm^{-3}; the change in magnitude for an 'on-axis' observer is $\Delta m_r \sim 1.2$, and for an 'off-axis' observer $\Delta m_r \sim 2.2$ for each order of magnitude change in the *n* parameter.

The light curves in Fig. 3 have afterglows which in each case are similar for an observer on the jet axis, i.e. the deceleration time, peak flux and peak time. The jet has a soft break that is determined by either the difference between the observation angle and the jet half-opening angle for a homogeneous jet, or the core angle for a jet with structure. A second break may be observed at later times, this is associated with the opening angle of the extended structure. A GRB afterglow for a homogeneous jet observed at the jet edge θ_j is half as bright and has a jet-break determined by the width of the jet $\sim 2\theta_j$; for the other structures the afterglow characteristics depend on the local jet energetics ϵ and Γ parameters.

Light curves for the jet structure models tested show that, where no sideways expansion is assumed and the jet-break is caused by the increase in the beaming angle beyond the jet edge, that the break seen in short GRB afterglows depends on the inclination. We expect a sharp break at very late times when the outflow becomes Newtonian, this is not included in our model. Fong et al. (2015) list four short GRBs with measured half-opening angles $3° \lesssim \theta_j \lesssim 8°$, and a further seven with lower limits; the narrowest of these lower limits is $\gtrsim 4°$ and the widest $\gtrsim 25°$. The average θ_j for short GRBs can be inferred by assuming a maximum jet half-opening angle; $\bar{\theta}_j = 16°^{+11}_{-10}$ for $\theta_{max} = 30°$, and $\bar{\theta}_j = 33°^{+38}_{-27}$ at the limit

$\theta_{\max} = 90°$; alternatively, Ghirlanda et al. (2016) found the short GRB population to be consistent with a jet opening angle of $3 \leq \theta_j \leq 6°$. We use a $\theta_j = 6°$ for homogeneous jets, consistent with both estimates, and fix this as the core angle for jets with extended structure. In these examples, the jet half-opening angle was inferred using $\Gamma^{-1}(t_b) \equiv \theta_j$. If the observed jet-break time t_b depends on inclination, as in our model for GRB afterglows, the break time cannot limit the full extent of jet structure. By assuming a range of jet parameters, the range of jet-break times can be reproduced by our model.

Additional features in the afterglow light curves for jets with extended structure appear at wider angles. For our parameters, these appear where the prompt emission is suppressed and the afterglow would be from a failed-GRB. Afterglows for the two-component model at angles $\theta_{obs} > \theta_c$ have an early peak flux and time determined by the local jet energy ϵ and Γ, respectively; a late bump is due to emission contribution from the bright core, the time of the bump is determined by the inclination, with higher inclinations resulting in a later bump time. A similar feature can be seen in the power-law structured-jet but as the energetics and Lorentz factor for the wider component are not uniform with angle, the early peak flux and time are unique. The afterglow for the Gaussian structured jet at comparable angles is dominated by the bright core emission at late times. For orphan afterglows in each structured jet case, the early rise time and peak are due to the contribution from the wide extended structure; a more energetic wide component leads to a brighter and more pronounced peak, while for a less energetic wide component, the orphan afterglow is dominated by the core emission at later times. As the observation angle increases, the contribution from the various components becomes indistinguishable, here we only show orphan afterglows until an observation angle of $40°$.

In all cases, we have assumed uniform baryon loading; if the baryon loading is more efficient towards the edge of a jet then ϵ and Γ will not have the same distribution. If the structure in a jet is due to baryon loading only, then the energy will be uniform; the afterglow for the various viewing angles will be brighter than the equivalent shown here as the peak flux depends on the energy. The peak time for the afterglow will be later for lower-Γ components; the prompt emission will be similarly suppressed.

4 PEAK FLUX/TIME

The 10^5 Monte Carlo distribution has a randomly determined inclination and distance given a GW detection, the same distribution is used with each jet structure, the afterglow from each jet structure model is evaluated at $1°$ intervals $0° \leq \theta_{obs} \leq 90°$; for efficiency, the model uses $N = 25$ and $M = 100$ ensuring jet structure is resolved. The peak magnitude for the light curve that corresponds to the jet structure at the randomly determined inclination is then selected and scaled for the distance. A histogram of the peak magnitude for jet EM counterparts brighter than magnitude 21, for GW detected mergers $\lesssim 300$ Mpc is shown in Fig. 4; the thick blue line is a GRB afterglow, the thin red line is a failed-GRB orphan afterglow, the black dashed line is an off-axis orphan afterglow. The fraction of each jet counterpart type, i.e. GRB afterglow, failed GRB afterglow, orphan afterglow, of the total number of $m \leq 21$ events are shown.

In Fig. 4, the peak of the distribution for GRB afterglows is that for a face-on NS–NS merger at the maximum detection distance ~ 300 Mpc. The structured jets have an extended distribution to fainter magnitudes when compared with the homogeneous jets, this is due to the lower energetics for observers $\theta_c < \theta_{obs}$. For the failed-GRB orphan afterglows from jets with structure, the distribution

for power-law structured and Gaussian structured jets has a wide plateau for the peak magnitudes due to the non-uniform energetics of the wider jet component. The two-component jet structure has a uniform energy distribution in the wide component, this gives a single sharp peak to the failed-GRB orphan afterglows.

The Monte Carlo results indicate the fraction of afterglow counterparts brighter than magnitude 21 depends on the jet structure model. For jets with extended structure to the limit of $25°$, we show that compared to a population of homogeneous jets with $\theta_j = 6°$ the fraction of bright jet counterparts is higher for two-component jets (equation 1) and power-law structured-jets (equation 2). GRB producing jets result in bright afterglows, with peak r-band magnitude $20 \gtrsim m_r \gtrsim 5$. Orphan afterglows brighter than magnitude 21, both from failed-GRBs and off-axis observations, are produced in ~ 12 per cent of cases for homogeneous jets, ~ 27 per cent for two-component jets, ~ 15 per cent of cases for power-law structured-jets and ~ 3.4 per cent for Gaussian jets. The brightest of these counterparts is $m_r \gtrsim 8$. The peak brightness depends on the jet kinetic energy and the fraction of events depends on the jet opening angle. For mergers that are close by, the prompt photon flux at angles $> \theta_c$ can be above the detection threshold; for two-component jets, where the ϵ distribution is generally flat in this region, a noticeable fraction of the counterparts will accompany faint GRBs. This can be seen by three peaks in the flux distribution for GRB afterglows.

The total fraction of EM counterparts brighter than magnitude 21 from the jet of GW detected mergers depends on the jet structure: for homogeneous jets we find ~ 13.6 per cent, for two-component jets ~ 30 per cent, for structured jets the fraction is ~ 37 per cent and Gaussian jets ~ 13 per cent. The fractions for an isotropic distribution to a distance of ~ 200 Mpc, the maximum for edge on NS–NS GW detection, are ~ 4.5 per cent, 11.8 per cent, 13.5 per cent and 4.1 per cent, respectively (homogeneous, two-component, power law and Gaussian); here GRB afterglows account for ~ 4.4 per cent, 3.4 per cent, 43.7 per cent and 53.7 per cent of the $m_r \leq 21$ counterpart fraction. In all cases, we consider the same structure parameters. The fraction of events brighter than magnitude 10, in each case, are dominated by GRB afterglows.

A corresponding histogram showing the peak time for each of the counterpart distributions is shown in Fig. 5. The colour and line style are the same as Fig. 4. The peak time distribution shows that for structured jets the GRB afterglows have a broader range of peak times than the homogeneous jet case. This is due to the non-uniform distribution of Lorentz factor for GRB producing jet components $> \theta_c$.

The jet counterparts $m_r \leq 21$, to GW detected mergers, typically peak at $t_p \lesssim 100$ d. The brightest counterparts peak very early $0.01 \lesssim t_p \lesssim 0.1$ d; orphan afterglows for a homogeneous jet peak typically at $t_p \sim 10$ d; failed-GRB and off-axis orphan afterglows typically peak at $t_p \sim 1$ d for power-law structured-jets and two-component jets; and Gaussian jets exhibit a bimodal distribution, due to the wide low-Γ extended jet structure, that peaks at $t_p \sim 0.25$ d and $t_p \sim 20$ d. The bimodal feature in the GRB afterglow distribution for two-component jets is due to the stepped boundary between the spine and sheath; detectable GRBs are produced outside of the core region $\theta_c = 6°$, these GRBs near the core edge have significantly lower Γ than those observed within the core angle; the second split in peak times for the two-component jets is due to the dominance of the off-axis core emission over the on-axis sheath emission, where on-axis emission will peak earlier. The apparent bimodality of the bright orphan afterglows for a homogeneous jet is a result of the sharp jet edge and uniformity of θ_j for the population as well as the numerical precision for changes of
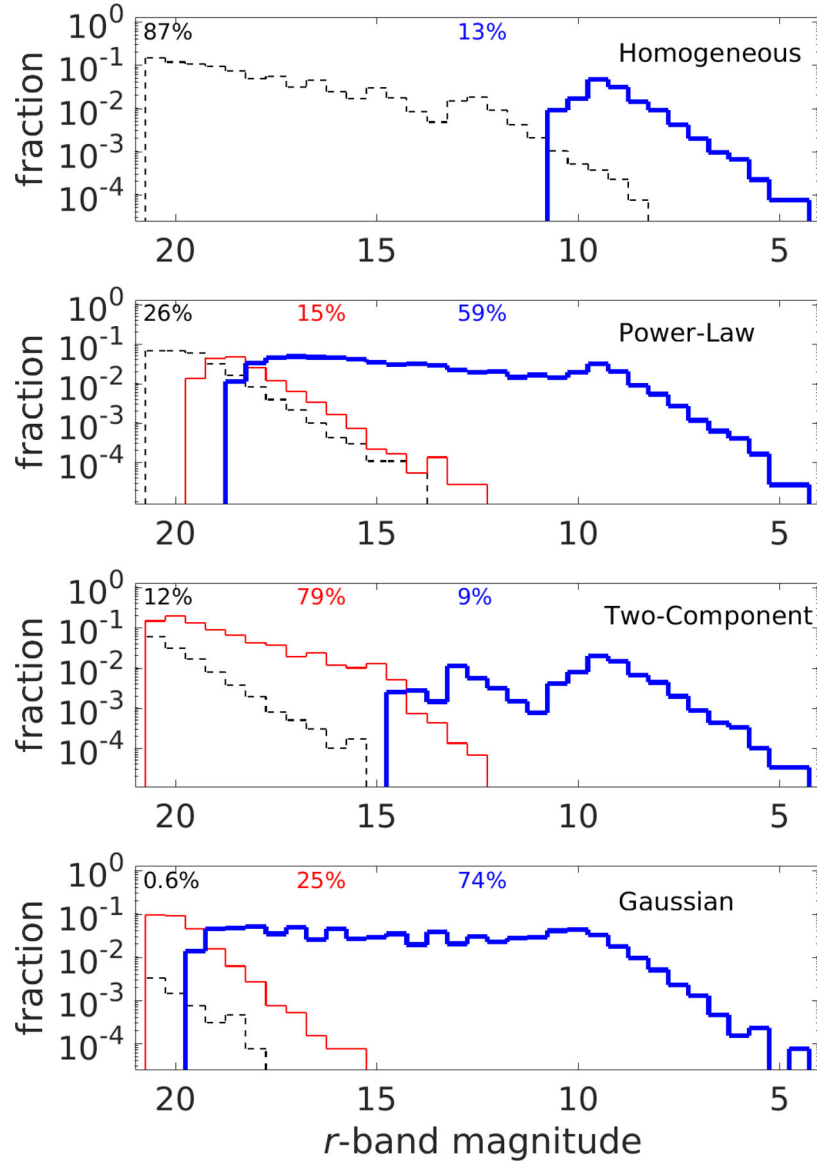
Figure 4. Peak magnitude for the afterglow brighter than 21 for a population of 10^5 GW detected mergers; the percentage of the total detected merger population for each type is homogeneous jets 13.6 per cent, power-law structured 36.9 per cent, two-component 30.0 per cent; and Gaussian 13.3 per cent. Blue thick line histogram is a GRB afterglow; red thin line histogram is an on-axis orphan (failed GRB) afterglow $\theta_{obs} < \theta_j$; black dashed line is an off-axis orphan afterglow $\theta_{obs} > \theta_j$. Percentages are the fraction of events brighter than magnitude 21 in each case.

inclination $<1°$; the bimodality would vanish for a population of jets with a distribution of θ_j or higher numerical resolution.

5 CONCLUSIONS

For jets from compact-stellar-mergers with a homogeneous structure, we have shown that wide opening angles $\theta_j \gtrsim 10°$ result in optical orphan afterglows, when viewed at the average GW detected merger inclination of $\sim38°$, that are brighter than the estimates for the equivalent peak flux from macronovae; note that this depends on the ambient density and jet energetics. We show that where jets have an extended structure to a limit of $\theta_j = 25°$, similar to the limit predicted by numerical simulations, the fraction of EM counterparts brighter than magnitude 21 can be 2–3 times that from a narrower homogeneous jet population. GW triggered searches for

EM counterparts could reveal a hidden population of failed-GRB orphan afterglows associated with wider jet structure, where the low energetics and Lorentz factor could suppress the prompt gamma-rays; we show light curve features in orphan afterglows that could indicate the presence of extended jet structure. Jet EM counterparts to GW detected NS–NS or BH–NS mergers will reveal the jet structure, Lorentz distribution and opening angle for short GRB jets.

We assumed a jet central axis observed isotropic blast energy of 2×10^{52} erg s^{-1}. A jet with a higher blast energy will result in an afterglow with a brighter peak magnitude. The various structured jet models naturally predict a range in observed total energetics that have a maximum at 2×10^{52} erg s^{-1}. The observed energetics of a jet, inferred from the prompt fluence and the peak of the afterglow, will appear lower for GRB afterglows seen at the jet edge for
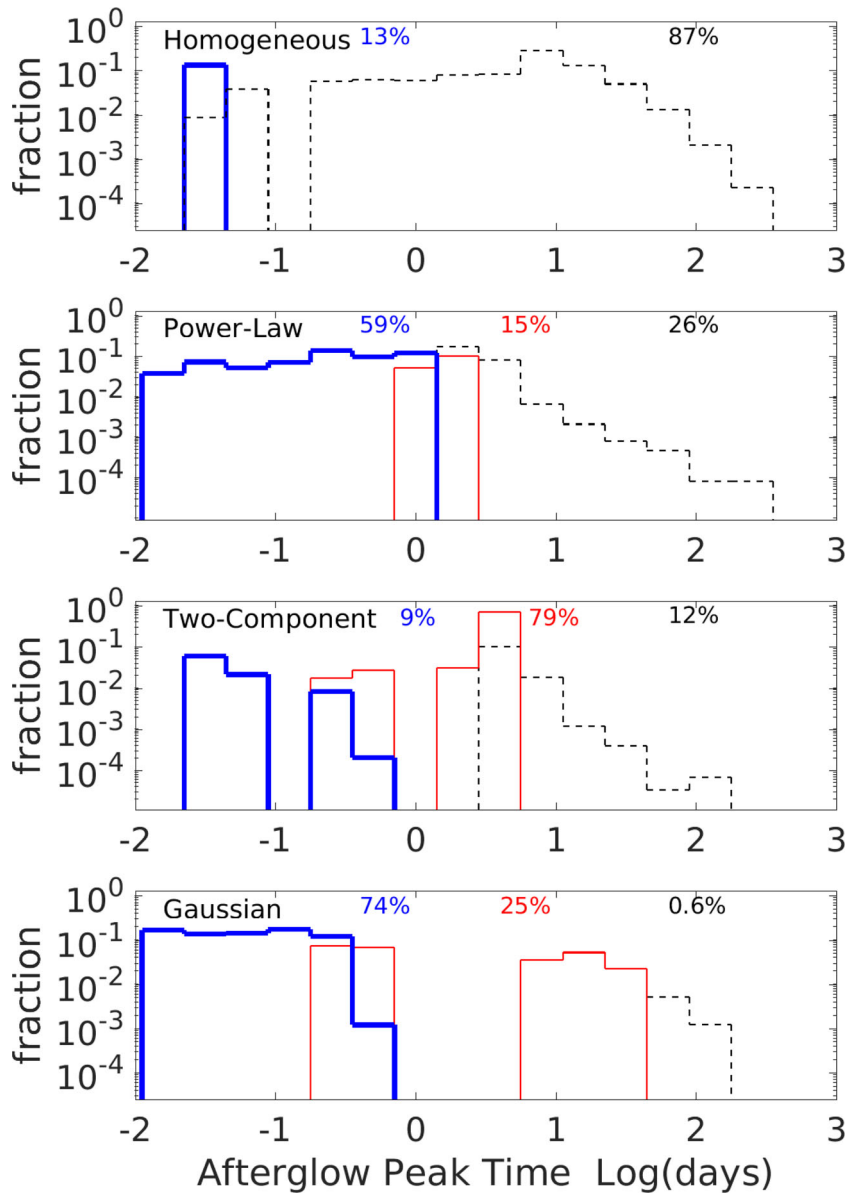
Figure 5. Peak time for the afterglows brighter than 21 for a population of 10^5 GW detected mergers. Blue thick line histogram is a GRB afterglow; red thin line histogram is an on-axis orphan (failed GRB) afterglow $\theta_{obs} < \theta_j$; black dashed line is an off-axis orphan afterglow $\theta_{obs} > \theta_j$. Percentages are the fraction of events brighter than magnitude 21 in each case.

homogeneous jets or outside the jet core for jets with a variable struc-
ture. Jets viewed at inclinations where most of the prompt emission
is suppressed may appear as X-ray flashes or low-luminosity GRBs;
in both cases the afterglow will appear dimmer and peak at later
times than for the on-axis afterglow. For jets observed at inclinations
comparable to the point where gamma-rays become suppressed, the
duration of the prompt emission will be longer due to the delayed
emission of the prompt photons from the low-Γ segments; the spec-
tra will have a strong thermal contribution. The longer duration of
such a GRB could result in misclassification as $T_{90} \gtrsim 2$ s.

The rate of NS–NS mergers within the advanced LIGO detection
volume is not known but values range from 0.2 to 200 yr^{-1} (e.g.
Aasi et al. 2013; Abbott et al. 2016). Metzger & Berger (2012)
made an estimate for the *Swift* detected short GRB with redshift rate
within this volume for NS–NS, 0.03 yr^{-1}; similarly, Coward et al.

(2012), Petrillo, Dietz & Cavaglià (2013), Siellez, Boër & Gendre
(2014) found a consistent rate for GW–GRBs within the aLIGO
volume, although the limits vary, and Fong et al. (2015) a merger-
rate of 8^{+47}_{-5} yr^{-1} which results in the same rate for *Swift*/BAT short
GRBs from jets with an opening angle of 16° and the *Swift*/BAT
field of view. The *Swift*/BAT field of view is ∼1.4 sr, therefore the
all-sky rate of short GRBs within the NS–NS detection volume is
∼0.27 yr^{-1}; by assuming that all *Swift*/BAT GRBs have the same
redshift distribution, the rate becomes ∼1.1 yr^{-1} as only 1/4 of
Swift/BAT short GRBs have a measured redshift. For each of our jet
models, we find the fraction that have peak afterglows brighter than
$m_r \leq 21$, of this fraction we find the percentage that are associated
with GRBs. If the all-sky rate of short GRBs within the NS–NS
LIGO detection volume is $0.27 \leq R_{SGRB} \leq 1.1$ yr^{-1} then the merger
rate will be: for homogeneous jets where 13 per cent of the GW

detected population are ≤ 21, and ~ 13 per cent of these are GRB afterglows, the fraction of the total population that produces GRBs is ~ 1.7 per cent giving a GW detectable merger rate of $15.9 \leq R_{\text{NS–NS}} \leq 63.5 \, \text{yr}^{-1}$; for two-component jets, the fractions of the population that results in a detected GRB is ~ 2.7 per cent, the merger rate is then $10 \leq R_{\text{NS–NS}} \leq 40 \, \text{yr}^{-1}$; for power-law jets, GRB fraction is 22 per cent, and the merger rate is $1.2 \leq N_{\text{NS–NS}} \leq 4.9 \, \text{yr}^{-1}$; for Gaussian jets, the GRB fraction is 9.6 per cent, and the merger rate $2.8 \leq R_{\text{NS–NS}} \leq 11.3 \, \text{yr}^{-1}$.

If we consider the number of potential counterparts that are brighter than $m_r \leq 21$ for each of these models with our parameters, we find that homogeneous jets will result in ~ 2–$8 \, \text{yr}^{-1}$, two-component jets will result in ~ 3–$12 \, \text{yr}^{-1}$, power-law jets ~ 0.4–$1.8 \, \text{yr}^{-1}$, and Gaussian jets ~ 0.4–$1.5 \, \text{yr}^{-1}$. Note, however that Bromberg et al. (2013) demonstrated that ~ 60 per cent of *Swift* short GRBs are non-collapsar in origin, this would reduce the estimated merger rates presented here.

Here, we have considered NS–NS mergers, if short GRBs are from BH–NS mergers only, then the rate will be a factor ~ 10 larger, where the maximum GW detection distance is approximately twice that for NS–NS mergers. As the merger ejecta from a BH–NS is not isotropically distributed, a larger fraction of the ejecta is on the rotational plane, the jet may not propagate through the merger ejecta; no significant cocoon phase will result in a wider jet. Any jet structure will be the result of the acceleration/formation mechanism. The fraction of bright EM jet counterparts to wide homogeneous jets from BH–NS mergers will be higher than those indicated here for NS–NS mergers; a homogeneous jet with $\theta_j \sim 25°$ will produce GRBs in ~ 27 per cent of GW detected mergers, whilst orphan and GRB afterglows with peak flux $m_r \leq 21$ will accompany $\lesssim 45$ per cent of GW detected mergers within the BH–NS GW detection volume $\sim 600 \, \text{Mpc}$. If the population is all BH–NS mergers with a $25°$ homogeneous jet, the merger rate will be $10 \leq R_{\text{BH–NS}} \leq 40 \, \text{yr}^{-1}$, and the number of bright GW-EM counterparts is 4.5–$18 \, \text{yr}^{-1}$. GW-EM counterparts from the jet will be detectable for a significant fraction of BH/NS–NS GW detected mergers; bright counterparts will typically peak $\lesssim 100$ d after the merger.

Electromagnetic follow-up of a GW trigger requires broad-band monitoring of the GW localization region; a bright optical transient from the jet afterglow, with these models, is expected within ~ 14 d. Optical telescopes with a limiting magnitude of ~ 21 (e.g. ZTF, Black GEM, GOTO) in joint observations with X-ray and γ-ray telescopes (e.g. *Swift*, *Fermi*, *MAXI*, *Chandra*) should perform intensive searches/monitoring within the first few weeks. At later times, any search or monitoring should be conducted by mid- to large-sized telescopes with higher sensitivity (e.g. Subaru HSC, LSST, LT) and radio/infrared observatories (e.g. VLA, ALMA), althogh high-energy monitoring could also reveal a late transient from an off-axis afterglow. For GW detected mergers that are significantly closer than $200 \, \text{Mpc}$, the search time-scales should be extended as any transients from structured or off-axis orphan afterglows will be brighter than the limiting detection thresholds for longer.

Given one well sampled GW-EM counterpart, the presence of extended jet structure could be revealed if the system is favourably inclined. An 'on-axis', within the jet core angle, afterglow would not reveal any signature of jet structure. However, afterglows at higher inclinations, or orphan afterglows, could reveal the presence of jet structure; an achromatic re-brightening would indicate a two-component, or a power-law structured-jet. A shallow decline or slowly brightening afterglow with a soft peak would indicate a Gaussian type jet structure observed at relatively high inclination (within

the jet opening angle). For an off-axis orphan afterglow, either sharp peak followed by a weak decay until a break or a shallow rise to a late peak can be used to indicate the existence of extended jet structure. Where the prompt emission has been fully suppressed, no X-ray flash or low-luminosity γ-ray burst, differentiating between an afterglow from within the jet opening angle and a genuine off-axis orphan in the cases of extended jet structure may not be possible.

ACKNOWLEDGEMENTS

REFERENCES

Aasi J. et al., 2013, Phys. Rev. D, 88, 062001
Abadie J. et al., 2010, Class. Quantum Gravity, 27, 173001
Abbott B. P. et al., 2016, Living Reviews in Relativity, 19, 1
Abbott B. P. et al., 2016, Phys. Rev. X, 6, 041015
Abbott B. P. et al., 2017, Phys. Rev. Lett., 118, 221101
Ackermann M. et al., 2016, ApJ, 823, L2
Aso Y. et al., 2013, Phys. Rev. D, 88, 043007
Band D. L., 2006, ApJ, 644, 378
Barkov M. V., Pozanenko A. S., 2011, MNRAS, 417, 2161
Beloborodov A. M., 2011, ApJ, 737, 68
Berger E., 2014, ARA&A, 52, 43
Berger E., Fong W., Chornock R., 2013, ApJ, 774, L23
Blandford R. D., Znajek R. L., 1977, MNRAS, 179, 433
Bogomazov A. I., Lipunov V. M., Tutukov A. V., 2007, Astron. Rep., 51, 308
Bromberg O., Nakar E., Piran T., Sari R., 2011, ApJ, 740, 100
Bromberg O., Nakar E., Piran T., Sari R., 2013, ApJ, 764, 179
Ciolfi R., Kastaun W., Giacomazzo B., Endrizzi A., Siegel D. M., Perna R., 2017, Phys. Rev. D, 95, 063016
Connaughton V. et al., 2016, ApJ, 826, L6
Coward D. M. et al., 2012, MNRAS, 425, 2668
Deaton M. B. et al., 2013, ApJ, 776, 47
Dietrich T., Ujevic M., 2017, Class. Quantum Gravity, 34, 105014
Dietrich T., Bernuzzi S., Ujevic M., Brügmann B., 2015, Phys. Rev. D, 91, 124041
Dionysopoulou K., Alic D., Rezzolla L., 2015, Phys. Rev. D, 92, 084064
Fong W., Berger E., Margutti R., Zauderer B. A., 2015, ApJ, 815, 102
Foucart F., Duez M. D., Kidder L. E., Scheel M. A., Szilagyi B., Teukolsky S. A., 2012, Phys. Rev. D, 85, 044015
Gao H., Ding X., Wu X.-F., Zhang B., Dai Z.-G., 2013, ApJ, 771, 86
Ghirlanda G., Nava L., Ghisellini G., Celotti A., Firmani C., 2009, A&A, 496, 585
Ghirlanda G. et al., 2016, A&A, 594, A84
Granot J., Panaitescu A., Kumar P., Woosley S. E., 2002, ApJ, 570, L61
Hascoët R., Beloborodov A. M., Daigne F., Mochkovitch R., 2014, ApJ, 782, 5
Hotokezaka K., Kiuchi K., Kyutoku K., Okawa H., Sekiguchi Yu-i. Shibata M., Taniguchi K., 2013, Phys. Rev. D, 87, 024001
Hotokezaka K., Nissanke S., Hallinan G., Lazio T. J. W., Nakar E., Piran T., 2016, ApJ, 831, 190
Jin Z. P., Yan T., Fan Y. Z., Wei D. M., 2007, ApJ, 656, L57
Jin Z.-P. et al., 2016, Nature Commun., 7, 12898
Jin Z.-P. et al., 2017, preprint (arXiv:1708.07008)
Kathirgamaraju A., Barniol Duran R., Giannios D., 2017, preprint (arXiv:1708.07488)

Kawaguchi K., Kyutoku K., Shibata M., Tanaka M., 2016, ApJ, 825, 52

Kisaka S., Ioka K., Takami H., 2015, ApJ, 802, 119

Kiuchi K., Sekiguchi Y., Shibata M., Taniguchi K., 2010, Phys. Rev. Lett., 104, 141101

Kobayashi S., Mészáros P., 2003, ApJ, 589, 861

Kobayashi S., Sari R., 2001, ApJ, 551, 934

Kobayashi S., Zhang B., 2003, ApJ, 582, L75

Kobayashi S., Piran T., Sari R., 1999, ApJ, 513, 669

Kobayashi S., Ryde F., MacFadyen A., 2002, ApJ, 577, 302

Kochanek C. S., Piran T., 1993, ApJ, 417, L17

Kumar P., Granot J., 2003, ApJ, 591, 1075

Kyutoku K., Ioka K., Okawa H., Shibata M., Taniguchi K., 2015, Phys. Rev. D, 92, 044028

Lamb G. P., Kobayashi S., 2016, ApJ, 829, 112

Lazzati D., Begelman M. C., 2005, ApJ, 629, 903

Lazzati D., Deich A., Morsony B. J., Workman J. C., 2017, MNRAS, 471, 1652

Lei W.-H., Zhang B., Liang E.-W., 2013, ApJ, 765, 125

Levinson A., Eichler D., 2003, ApJ, 594, L19

Li L.-X., Paczyński B., 1998, ApJ, 507, L59

Lipunov V. M., Postnov K. A., Prokhorov M. E., 2001, Astron. Rep., 45, 236

Lithwick Y., Sari R., 2001, ApJ, 555, 540

Loeb A., 2016, ApJ, 819, L21

Lyutikov M., Blandford R., 2002, in Ouyed R., ed, Beaming and Jets in Gamma Ray Bursts. p. 146

Mészáros P., Rees M. J., 1997, ApJ, 476, 232

Metzger B. D., Berger E., 2012, ApJ, 746, 48

Metzger B. D., Bauswein A., Goriely S., Kasen D., 2015, MNRAS, 446, 1115

Mochkovitch R., Hernanz M., Isern J., Martin X., 1993, Nature, 361, 236

Morsony B. J., Lazzati D., Begelman M. C., 2010, ApJ, 723, 267

Mundell C. G. et al., 2013, Nature, 504, 119

Nagakura H., Hotokezaka K., Sekiguchi Y., Shibata M., Ioka K., 2014, ApJ, 784, L28

Nakar E., 2007, Phys. Rep., 442, 166

Nakar E., Piran T., 2002, MNRAS, 330, 920

Nakar E., Piran T., 2011, Nature, 478, 82

Nakar E., Piran T., 2017, ApJ, 834, 28

Narayan R., Paczynski B., Piran T., 1992, ApJ, 395, L83

Nissanke S., Holz D. E., Hughes S. A., Dalal N., Sievers J. L., 2010, ApJ, 725, 496

Nissanke S., Kasliwal M., Georgieva A., 2013, ApJ, 767, 124

Panaitescu A., 2005, MNRAS, 363, 1409

Pe'er A., Mészáros P., Rees M. J., 2005, ApJ, 635, 476

Peng F., Königl A., Granot J., 2005, ApJ, 626, 966

Perna R., Lazzati D., Giacomazzo B., 2016, ApJ, 821, L18

Pescalli A., Ghirlanda G., Salafia O. S., Ghisellini G., Nappo F., Salvaterra R., 2015, MNRAS, 447, 1911

Petrillo C. E., Dietz A., Cavaglià M., 2013, ApJ, 767, 140

Piran T., 2004, Reviews of Modern Physics, 76, 1143

Piran T., Shemi A., Narayan R., 1993, MNRAS, 263, 861

Popham R., Woosley S. E., Fryer C., 1999, ApJ, 518, 356

Rees M. J., Meszaros P., 1992, MNRAS, 258, 41P

Rees M. J., Meszaros P., 1994, ApJ, 430, L93

Rezzolla L., Giacomazzo B., Baiotti L., Granot J., Kouveliotou C., Aloy M. A., 2011, ApJ, 732, L6

Rossi E., Lazzati D., Rees M. J., 2002, MNRAS, 332, 945

Rossi E. M., Lazzati D., Salmonson J. D., Ghisellini G., 2004, MNRAS, 354, 86

Rosswog S., Davies M. B., Thielemann F.-K., Piran T., 2000, A&A, 360, 171

Ruffert M., Janka H.-T., 2001, A&A, 380, 544

Rybicki G. B., Lightman A. P., 1979, Radiative Processes in Astrophysics. Wiley-Interscience, New York, p. 393

Salmonson J. D., 2003, ApJ, 592, 1002

Sari R., Piran T., 1999, ApJ, 520, 641

Sari R., Piran T., Narayan R., 1998, ApJ, 497, L17

Sari R., Piran T., Halpern J. P., 1999, ApJ, 519, L17

Savchenko V. et al., 2016, ApJ, 820, L36

Schutz B. F., 2011, Class. Quantum Gravity, 28, 125023

Shapiro S. L., 2017, Phys. Rev., 95, 10

Siellez K., Boër M., Gendre B., 2014, MNRAS, 437, 649

Steele I. A., Mundell C. G., Smith R. J., Kobayashi S., Guidorzi C., 2009, Nature, 462, 767

Tanaka M., 2016, Adv. Astron., 2016, 634197

Tanaka M., Hotokezaka K., Kyutoku K., Wanajo S., Kiuchi K., Sekiguchi Y., Shibata M., 2014, ApJ, 780, 31

Tanvir N. R., Levan A. J., Fruchter A. S., Hjorth J., Hounsell R. A., Wiersema K., Tunnicliffe R. L., 2013, Nature, 500, 547

Thompson C., Mészáros P., Rees M. J., 2007, ApJ, 666, 1012

van Eerten H. J., MacFadyen A. I., 2012, ApJ, 751, 155

van Putten M. H. P. M., Levinson A., 2003, ApJ, 584, 937

Verrecchia F. et al., 2017, ApJL, preprint (arXiv:1706.00029)

Vlahakis N., Peng F., Königl A., 2003, ApJ, 594, L23

Wanderman D., Piran T., 2015, MNRAS, 448, 3026

Wei D. M., Jin Z. P., 2003, A&A, 400, 415

Wollaeger R. T. et al., 2017, MNRAS, preprint (arXiv:1705.07084)

Yamamoto T., Shibata M., Taniguchi K., 2008, Phys. Rev. D, 78, 064054

Yamazaki R., Asano K., Ohira Y., 2016, Prog. Thero. Exp. Phys., 2016, 051E01

Yonetoku D., Murakami T., Nakamura T., Yamazaki R., Inoue A. K., Ioka K., 2004, ApJ, 609, 935

Zhang B., 2016, ApJ, 827, L31

Zhang Q. S., Li Y., 2012, ApJ, 750, 11

Zhang B., Mészáros P., 2002, ApJ, 571, 876

Zhang B., Mészáros P., 2004, Int. J. Mod. Phys. A, 19, 2385

Zhang B., Yan H., 2011, ApJ, 726, 90

Zhang W., Woosley S. E., MacFadyen A. I., 2003, ApJ, 586, 356

Zhang W., Woosley S. E., Heger A., 2004, ApJ, 608, 365

This paper has been typeset from a TEX/LATEX file prepared by the author.